



UNIVERSITY OF TRENTO
DEPARTMENT OF PHYSICS
BACHELOR'S DEGREE IN PHYSICS

~ . ~

ACADEMIC YEAR 2023–2024

BUBBLES IN A FERROMAGNETIC SUPERFLUID

Supervisor
Dr. Alessandro ZENESINI

Graduate Student
Giorgio MICAGLIO
227051

FINAL EXAMINATION DATE: March 10, 2025

A mamma e papà

Acknowledgments

I would like to thank all of my friends.

Abstract

This thesis analyses an experiment observing bubbles in a ferromagnetic superfluid formed through false vacuum decay. The aim of this work is to characterize the bubbles in order to retrieve their most important properties and relating them to the parameters of the experiment.

Contents

Introduction	1
1 Theoretical background	3
1.1 Ideal Bose gas	3
1.2 Gross-Pitaevskii equation	5
1.3 Two-component spin mixture	5
1.4 Coherently coupled mixture	7
1.4.1 Ferromagnetism	7
1.5 False vacuum decay and bubble formation	7
2 Data analysis	9
2.1 Experimental platform	9
2.2 Raw data	10
2.2.1 Bubble fit parameters	10
2.2.2 Shot sorting	12
2.3 Parameters analysis	12
2.4 Spectral analysis	14
2.4.1 FFT and ACF definition	14
2.4.2 FFT and ACF analysis on sequences	15
2.4.3 ACF analysis on all shots	16
Conclusions	23
A ACF models	25
A.1 Pure sinusoid	25
Bibliography	27
List of Figures	30

CONTENTS

Introduction

This thesis originates from the first experimental observation of False Vacuum Decay (FVD), made by the Pitaevskii BEC Center laboratories of the University of Trento and presented in Ref. [3].

INTRODUCTION

Chapter 1

Theoretical background

In this chapter we will briefly discuss the theoretical background used when dealing with two-component coherently coupled spin mixtures of BECs. Since we are dealing with a many-body quantum problem, the standard approach is to use a quantum field to describe the state of the condensate. This leads directly to the Gross-Pitaevskii equation, which will be the starting point of this discussion, after a quick review of the ideal Bose gas. The following content is mostly based on Refs. [2] and [1].

1.1 Ideal Bose gas

The simplest way to treat the ideal Bose gas (a quantum system of non-interacting bosons) is by relying on the grand-canonical ensemble.

Let us then recall the probability of the system having a number of particles N' and energy E_k when in contact with a reservoir of temperature T and chemical potential μ :

$$P_{N'}(E_k) = e^{\beta(\mu N' - E_k)},$$

with $\beta = 1/(k_B T)$, from which one can build the *grand-canonical partition function*

$$\mathcal{Z}(\beta, \mu) = \sum_{N'=0}^{\infty} \sum_k P_{N'}(E_k) = \sum_{N'=0}^{\infty} e^{\beta\mu N'} Q_{N'}(\beta), \quad (1.1)$$

where $Q_{N'}$ is the canonical partition function associated to a system of N' (fixed) particles. From the partition function, the physical properties of the system are derived through the calculation of the grand-canonical potential

$$\Omega = E - TS - \mu N = -k_B T \log \mathcal{Z}. \quad (1.2)$$

In the case of a non-interacting system, the total Hamiltonian is $H = \sum_i H_i$, where the single-particle Hamiltonian solves the eigenvalue problem $H_i \phi_i(\mathbf{r}) = \epsilon_i \phi_i(\mathbf{r})$. In this setting, each energy level ϵ_i is occupied by n_i particles, and thus the total number of particles and the total energy are

$$N' = \sum_i n_i, \quad E_k = \sum_i \epsilon_i n_i.$$

The partition function of Eq. (1.1) becomes easy to compute, yielding

$$\begin{aligned}\mathcal{Z}(\beta, \mu) &= \sum_{n_0=0}^{\infty} \sum_{n_1=0}^{\infty} \dots e^{\beta\mu \sum_i n_i} e^{-\beta \sum_i \epsilon_i n_i} = \left(\sum_{n_0} e^{\beta\mu n_0} e^{-\beta\epsilon_0 n_0} \right) \left(\sum_{n_1} e^{\beta\mu n_1} e^{-\beta\epsilon_1 n_1} \right) = \\ &= \prod_i \sum_{n_i} \left[e^{\beta(\mu - \epsilon_i)} \right]^{n_i} = \prod_i \frac{1}{1 - e^{\beta(\mu - \epsilon_i)}}.\end{aligned}$$

Note that the condition $\mu < \epsilon_0$ must be satisfied for the convergence of the series. It is interesting to study the total number of particles, which can be obtained from the potential of Eq. (1.2):

$$N = \langle N' \rangle = -\frac{\partial \Omega}{\partial \mu} = k_B T \frac{\partial \log \mathcal{Z}}{\partial \mu} = \sum_i \frac{1}{e^{\beta(\epsilon_i - \mu)} - 1} = \sum_i \langle n_i \rangle,$$

hence revealing the famous *Bose-Einstein distribution*

$$\langle n_i \rangle = \frac{1}{e^{\beta(\epsilon_i - \mu)} - 1}.$$

The occupation number of the ground state is $N_0 = \langle n_0 \rangle$ and the remaining particles are called the thermal component $N_T = N - N_0$.

The origin of the Bose-Einstein condensation phenomenon is that $N_0 \rightarrow \infty$ when $\mu \rightarrow \epsilon_0$. In particular, at a fixed temperature T , the function $N_T(\mu)$ has a maximum N_c at $\mu = \epsilon_0$, while N_0 is divergent. This implies that:

- if $N_c > N$, then the normalization condition $N = N_0 + N_T$ is satisfied for values of $\mu < \epsilon_0$ and N_0 is negligible (no condensation);
- if $N_c = N$, it means that we are at the critical temperature T_c defined by $N_T(T = T_c, \mu = \epsilon_0) = N$. Since N_T is an increasing function of T , the previous scenario corresponds to $T > T_c$;
- if $N_c < N$ (or $T < T_c$), the contribution of N_0 is crucial for the normalization and thus the condensation happens.

In a finite box of volume V , where the lowest energy eigenvalue is $\epsilon_0 = 0$, the condensate fraction for $T < T_c$ is expressed by

$$\frac{N_0}{N} = 1 - \left(\frac{T}{T_c} \right)^{3/2}.$$

Since $N_0 \approx 0$ for $T > T_c$, the function has a discontinuity of its derivative at the critical temperature: a typical symptom of phase transitions.

The behaviour is similar for a system trapped in an external harmonic potential, where the condensate fraction is

$$\frac{N_0}{N} = 1 - \left(\frac{T}{T_c} \right)^3$$

and the critical temperature depends on the oscillation frequencies.

1.2 Gross-Pitaevskii equation

For a 1D single-component BEC, namely made of only one species of N indistinguishable bosons, one can use a single wavefunction $\psi(x, t)$ to describe its ground state (GS) by exploiting a mean-field approximation, thus revealing the Gross-Pitaevskii equation (GPE):

$$i\hbar \frac{\partial \psi(x, t)}{\partial t} = \left[-\frac{\hbar^2}{2m} \nabla^2 + V(x, t) + g|\psi(x, t)|^2 \right] \psi(x, t). \quad (1.3)$$

The unusual term in this equation is the one proportional to the square modulus of the wavefunction through the constant g , called the *contact interaction constant*, that describes the interactions between bosons. In fact, for an ideal gas of non-interacting bosons, $g = 0$ and one retrieves the standard Schrödinger equation, but this situation is not realistic for our purposes. The interaction constant can be written in terms of the boson-boson scattering length a , a typical property of elastic collisions, by

$$g = \frac{4\pi\hbar^2}{m} a,$$

with $g > 0$ for a stable BEC (for $g < 0$ the system is unstable and collapses on itself).

The GPE can be written in its stationary form as

$$\left[-\frac{\hbar^2}{2m} \nabla^2 + V(x) + g|\psi(x)|^2 \right] \psi(x) = \mu\psi(x), \quad (1.4)$$

where $\mu \approx \frac{\partial E}{\partial N}$ is the chemical potential and accounts for the energy contribution of a single particle. Spatial properties of the condensate can arise from this equation, especially in the case of $N \gg 1$ and when the interaction term is dominating. By neglecting the kinetic energy term from Eq. (1.4), one easily gets the stationary solution

$$|\psi(x)|^2 = n(x) = \frac{\mu - V(x)}{g},$$

where $n(x)$ is the density distribution, and the association of the latter with the square modulus of the wavefunction leads to the normalization condition $\int |\psi(x)|^2 dx = N$. A relevant case is when the external potential is harmonic, yielding a parabolic distribution

$$n(x) = \frac{\mu - \frac{1}{2}m\omega^2x^2}{g} = 0 \quad \Leftrightarrow \quad x = R_{\text{TF}} = \sqrt{\frac{2\mu}{m\omega^2}}, \quad (1.5)$$

with R_{TF} being the Thomas-Fermi radius, a parameter indicating the spatial confinement of the condensate.

1.3 Two-component spin mixture

When the system is composed of two different species (a and b), Eq. (1.4) splits into two coupled stationary GPEs:

$$\begin{aligned} \left[-\frac{\hbar^2}{2m} \nabla^2 + V(x) + g_{aa}|\psi_a(x)|^2 + g_{ab}|\psi_b(x)|^2 \right] \psi_a(x) &= \mu_a \psi_a(x), \\ \left[-\frac{\hbar^2}{2m} \nabla^2 + V(x) + g_{ab}|\psi_a(x)|^2 + g_{bb}|\psi_b(x)|^2 \right] \psi_b(x) &= \mu_b \psi_b(x). \end{aligned}$$

This is due to the possibility of collisions not only between bosons a - a or b - b , but also of the type a - b , thus producing three interaction constants g_{aa} , g_{bb} , g_{ab} . Depending on those constants' values, the system can assume different behaviours and GS configurations.

For example, take the case of a flat box potential in a total fixed volume V , yielding constant densities. Letting $n_a = |\psi_a|^2$ and $n_b = |\psi_b|^2$, we can express the energy density in the following way:

$$\mathcal{E} = \frac{1}{2}g_a n_a^2 + \frac{1}{2}g_b n_b^2 + g_{ab}n_a n_b - \mu_a n_a - \mu_b n_b,$$

where the first three terms represent the interactions between particles of the same type and between different ones, while the last two terms account for the chemical potentials. Now, we state that the system is thermodynamically stable and miscible if and only if the Hessian of \mathcal{E} with respect to n_a and n_b is positive-definite. The calculation is straight-forward:

$$H = \begin{bmatrix} \frac{\partial^2 \mathcal{E}}{\partial n_a^2} & \frac{\partial^2 \mathcal{E}}{\partial n_a \partial n_b} \\ \frac{\partial^2 \mathcal{E}}{\partial n_a \partial n_b} & \frac{\partial^2 \mathcal{E}}{\partial n_b^2} \end{bmatrix} = \begin{bmatrix} g_a & g_{ab} \\ g_{ab} & g_b \end{bmatrix} > 0 \quad \Leftrightarrow \quad \begin{cases} g_a > 0 \\ g_b > 0 \\ g_a g_b > g_{ab}^2 \end{cases}.$$

The first two conditions ensure that neither a nor b collapse, while the latter expresses the condition for miscibility. Intuitively, if g_{ab} is small with respect to the other constants, it means that the two species do not interact much one with the other, thus letting themselves mix and spatially overlap. On the other hand, if g_{ab} is big (and positive), they strongly repulse and undergo a phase separation. From now on, only repulsive interactions will be considered, so the only possibilities will be immiscible or miscible (no collapse).

In the more general case of a non-uniform trapping potential, the densities depend from the position and the distributions are correlated with the interaction constants. Considering the harmonic trap and the miscible case, if $g_a > g_b$ then the species b will be confined in a small central region, while the species a will occupy more space. This is shown in the lower section of

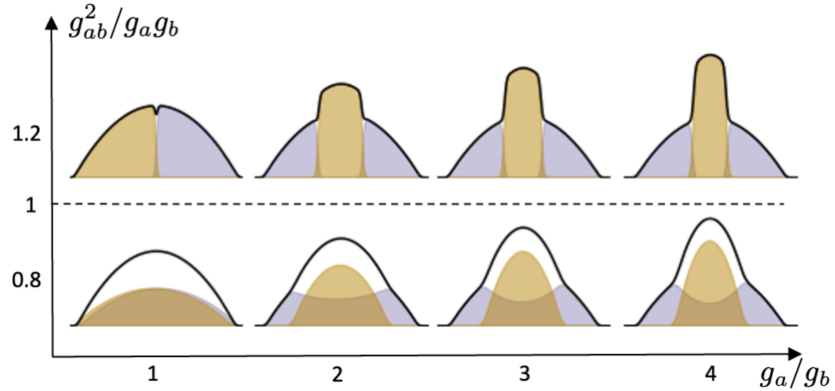


Figure 1.1: GPE simulation of a two-component balanced mixture in a harmonic potential. The shaded purple region shows the density distribution of population a and the yellow one the population b . Here, a small magnetic field is used to break the left-right simmetry. The total density profile is drawn in black.

Fig. 1.1, while the upper section shows the immiscible case and the buoyancy (again, $g_a > g_b$). One notes that the total density profile is not Thomas-Fermi anymore when $g_a \neq g_b$.

1.4 Coherently coupled mixture

When the system is composed of two species of the same atom, such as two hyperfine states, the dynamics become more interesting because of the possible interconversion processes. One possibility is to use a homogeneous microwave radiation, which couples the two internal states $|a\rangle$ and $|b\rangle$, of the type

$$\Omega_R(t) \exp\left\{-i\omega_{\text{cpl}}t + \phi\right\}, \quad \text{with } \omega_{\text{cpl}} = \omega_{ab} + \delta_B.$$

Here, ω_{ab} is the transition frequency between the two coupled states, and in the case of two hyperfine states of the same angular momentum level it includes the linear Zeeman splitting of a small external magnetic field. The coupling frequency ω_{cpl} differs from ω_{ab} by a parameter δ_B called *detuning*.

1.4.1 Ferromagnetism

In this scenario, the system exhibits magnetic properties, namely a phase transition from *paramagnetism* to *ferromagnetism*.

1.5 False vacuum decay and bubble formation

Given the asymmetric double well

$$V_{\text{MF}}(Z) = -\delta_{\text{eff}}Z + \frac{|k|n}{2}Z^2 - \Omega_R \sqrt{1-Z^2} \cos \phi$$

describing the spin channel mean-field energy landscape of the condensate (Fig. 1.2), the metastable state A in which all atoms are in the state $|\uparrow\rangle$ is called False Vacuum (FV), since it is not the true ground state. The possibility of tunneling to the state B arises from the fact that the bubble

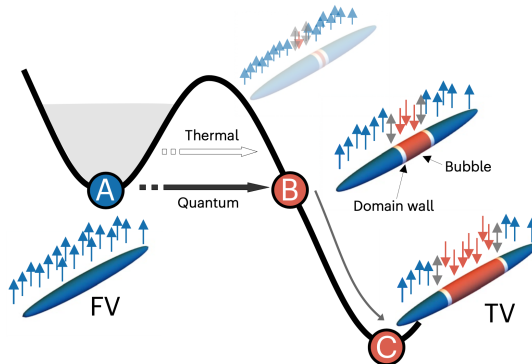


Figure 1.2: Mean field energy and bubble formation.

formation has an energy cost due to the kinetic contribution of the interaction on the interface (domain wall) between atoms $|\uparrow\rangle$ and $|\downarrow\rangle$. However, when a sufficient number of atoms in the core region flips to $|\downarrow\rangle$, the energy gain compensates the kinetic cost and the tunneling can occur

CHAPTER 1. THEORETICAL BACKGROUND

resonantly from A to B. Once happened, the system is not in a metastable state anymore, hence the decaying into C, the True Vacuum (TV), via bubble expansion.¹

What is interesting to study is the energy dissipation of the decay during the expansion. The key point is that since the coherent coupling prohibits the system to emit photons, the energy must dissipate through the spin and/or density channel, possibly with waves. Investigating this phenomenon is the purpose of this thesis' data analysis.

¹Note that the TV is not composed of all atoms $|\downarrow\rangle$. This is because while the $|\downarrow\rangle$ state is energetically lower in the high-density core region, the situation is opposite in the low-density tails.

Chapter 2

Data analysis

In this chapter we describe the experimental platform in which the measurements were carried out (Ref. [3]) and we will then proceed with the FFT and ACF data analysis. The code for the analysis was written in the **Python** programming language.

2.1 Experimental platform

The experimental platform is composed of a bosonic gas of ^{23}Na atoms, optically trapped and cooled below the condensation temperature. The initial spin state in which the system is prepared is $|F, m_F\rangle = |2, -2\rangle = |\uparrow\rangle$, with F being the total angular momentum of the atom and m_F its projection on the quantization axis. The $|\uparrow\rangle$ state is then coupled to $|1, -1\rangle = |\downarrow\rangle$ through microwave radiation with amplitude Ω_R . The relevant scattering lengths concerning the two states are $a_{\uparrow} = 64.3a_0$, $a_{\downarrow} = 54.5a_0$ and $a_{\uparrow\downarrow} = 64.3a_0$.

The trapping potential is harmonic in all three directions, but strongly asymmetric concerning the radial (ρ) and axial (x) directions. In fact, the trapping frequencies are respectively $\nu_{\rho} = 2$ kHz and $\nu_x = 20$ Hz, yielding an elongated system (cigar-shaped) with inhomogeneous density. The spatial size of the system is given by the Thomas-Fermi radii $R_{\rho} = 2$ μm and $R_x = 200$ μm , calculated with Eq. (1.5). This particular setup is helpful for suppressing the radial spin dynamics of the condensate and thus reducing it from a 3D system of density $n_{3D}(r_{\perp}, x)$ to a 1D system of linear density $n(x)$, with the only difference being the renormalization of the interaction constant

$$\delta g \rightarrow k = \frac{2}{3} \frac{n_{3D}}{n} \delta g.$$

In order to extract the density distribution, the two spin states are treated independently one from another, and a spin-selective imaging process is performed. Then, an integration along the transverse direction is carried out, obtaining two 1D density profiles $n_{\uparrow}(x)$ and $n_{\downarrow}(x)$, from which one can extract the relative magnetization

$$Z(x) = \frac{n_{\uparrow}(x) - n_{\downarrow}(x)}{n_{\uparrow}(x) + n_{\downarrow}(x)}. \quad (2.1)$$

Due to the quantum nature of the system, once imaged the condensate loses its spatial information and it has to be prepared back in the initial state, allowing for another measurement.

2.2 Raw data

Raw data is organized in a hierarchical system. At a fixed instant, the condensate's measured data are called a *shot* (it refers to the imaging process). Each shot is part of a series of them that can be analyzed as the time evolution of a single system: this series is called a *sequence*. Eventually, during a *day* of measurements, many sequences may be collected, and a selection of them will be studied in the following analysis. For each sequence, the experimental data contains also the radiation coupling Ω_R in a range between $2\pi \times 200$ Hz and $2\pi \times 800$ Hz (it changes from one day of measurements to another) and the detuning δ in a range between $2\pi \times 100$ Hz and $2\pi \times 600$ Hz. For each shot, the experimental waiting time t is saved and it provides information on the time interval passed before the imaging process, ranging from 1 ms to 300 ms.

A shot contains all the information on the system after waiting for a time t , including the two population densities, $n_{\uparrow}(x)$ for the atoms in the state $|\uparrow\rangle$ and $n_{\downarrow}(x)$ for the atoms in the state $|\downarrow\rangle$, distributed on a length scale from 0 to 400 pixels. The spatial resolution of the image is 1 pixel = $1.025 \mu\text{m} \approx 1 \mu\text{m}$, so the two length units will often be used interchangeably. The magnetization data $Z(x)$ is calculated with Eq. (2.1) and, by definition, composed of a series of values ranging from -1 (all atoms in the state $|\downarrow\rangle$) to 1 (all atoms in the state $|\uparrow\rangle$).

Our focus here is to characterize the bubble properties in relation to Ω_R , δ , t by utilizing the magnetization of the system. First, we need to extract the spatial parameters of the bubble in order to locate it in each shot, then we will proceed with the study of its evolution.

2.2.1 Bubble fit parameters

In order to localize the bubble in a shot, the most interesting parameters to retrieve are the bubble center x_0 and its width σ_B . However, not all shots contain a bubble, namely the ones taken when the bubble was not formed yet. We can easily classify the two types of shots by computing the magnetization average in the central region and using a threshold value, set to $Z_{\text{thr}} = -0.2$.

To parametrize the bubble, the magnetization data is fitted with a double-arctangent function

$$Z_{\text{fit}}(x) = -A \left[\frac{2}{\pi} \arctan\left(\frac{x - c_1}{w_1}\right) - \frac{2}{\pi} \arctan\left(\frac{x - c_2}{w_2}\right) \right] + \Delta, \quad (2.2)$$

where c_1 and c_2 are the centers' positions of the arctangent "shoulders", and w_1 and w_2 are their characteristic widths. Then, for a better result, a further fit is performed on each shoulder with a single-arctangent function

$$Z_{\text{fit}}(x) = -A \frac{2}{\pi} \arctan\left(\frac{x - c_{1,2}}{w_{1,2}}\right) + \Delta, \quad (2.3)$$

yielding the shoulder center position $c_{1,2}$. Eventually, we obtain the bubble center position $x_0 = (c_1 + c_2)/2$ and the bubble width $\sigma_B = c_2 - c_1$.

While this routine is very accurate for determining the shoulder profile and hence the bubble width, the transition between the shoulders and the inside region (the bubble itself) shows no continuity in many shots. In order to capture the entire profile and especially the boundaries of the inside region, we can fit the data with a continuous piecewise function made of two

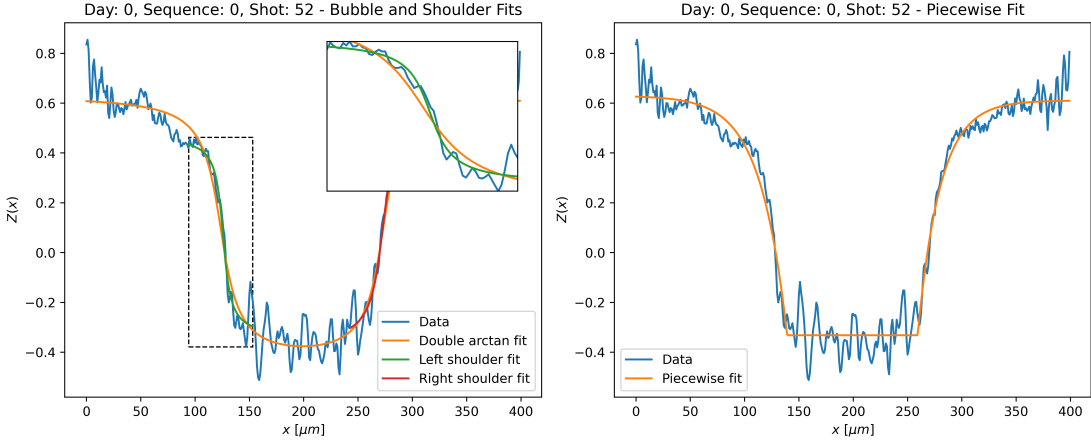


Figure 2.1: Example of fit results performed on a shot. First, the data is fitted with the double-arctangent function of Eq. (2.2), then each shoulder is fitted with a single-arctangent, namely the one of Eq. (2.3). This ensures a better estimation of the shoulder centers and thus of the bubble width. Eventually, a last fit is done with the piecewise function of Eq. (2.4), in order to capture the inside/outside discontinuity and the exponential tails.

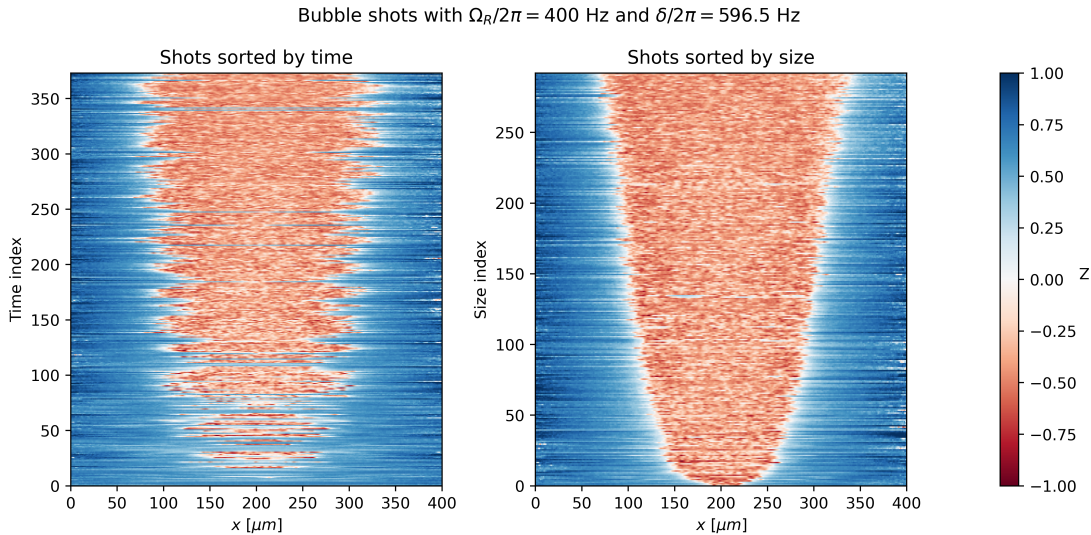


Figure 2.2: Example of initial shot sorting based on experimental waiting time (on the left) and final sorting based on bubble width σ_B (on the right) for all shots with $\Omega_R/2\pi = 400$ Hz and $\delta/2\pi = 596.5$ Hz. The σ_B parameter is estimated from the previous fitting procedure, and the no-bubble shots ($\sigma_B = 0$) are removed from the right plot. The data is colored by mapping positive magnetization to blue and negative magnetization to red.

exponential tails and a constant value in the middle, such as

$$Z_{\text{fit}}(x) = \begin{cases} (A - \Delta_1) \exp\left(\frac{x-x_1}{w_1}\right) + \Delta_1 & \text{for } x < x_1 \\ A & \text{for } x_1 < x < x_2 , \\ (A - \Delta_2) \exp\left(-\frac{x-x_2}{w_2}\right) + \Delta_2 & \text{for } x > x_2 \end{cases} \quad (2.4)$$

yielding also the characteristic widths of the tails w_1 and w_2 .

An example of fitting with the arctangent and stepwise exponential functions is provided in Fig. 2.1.

2.2.2 Shot sorting

Once the bubble width σ_B is retrieved, it is useful to order the shots in a sequence by this parameter. This process lets us display the system evolution, in contrast to the original shot ordering based on the experimental time waited before observing the bubble. The reason why we are more interested in the size dependence is that the bubble formation event is a stochastic process (the tunneling through the mean-field energy barrier), and the time at which a bubble forms is not determined. However, theory suggests that once the bubble is formed, its evolution (the decay from FV to TV) is determined. An example of sorting by both time and size is shown in Fig. 2.2 with a colormap displaying the magnetization profiles (blue is for positive Z and red for negative Z).

2.3 Parameters analysis

In order to look at the distribution of the bubble parameters versus the experimental time or the bubble size, we decide to group all shots by the radiation coupling Ω_R (ignoring the detuning δ) and plot the bubble width and tail width, the latter being the left-right average $(w_1 + w_2)/2$ from Eq. (2.4). An approach to this might be the one of ordering the shots by time or size

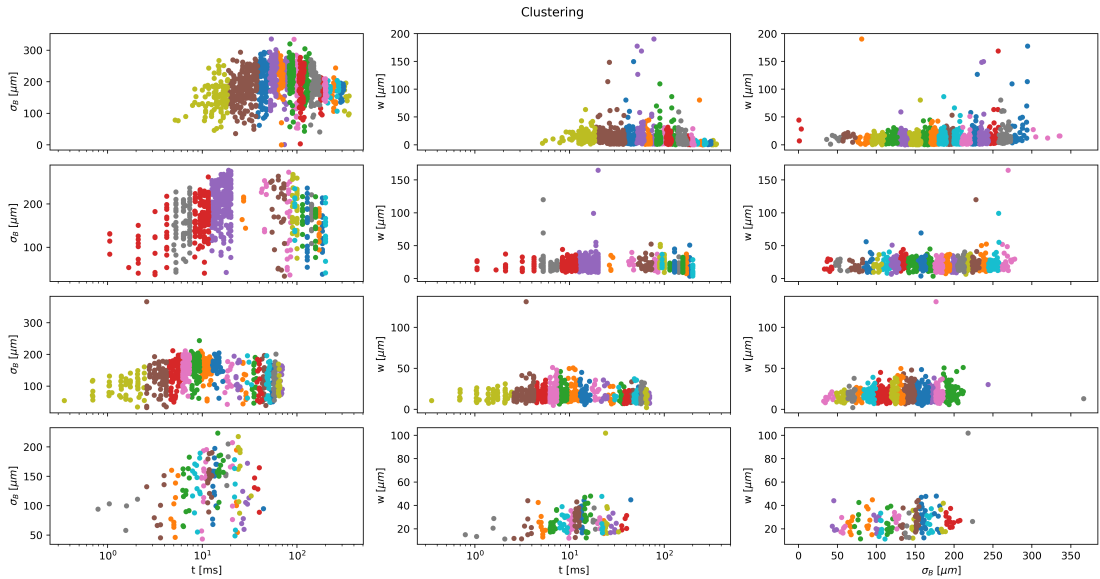


Figure 2.3: Data clustering with the K-Means algorithm and $n_{\text{clusters}} = 20$ based only on t (first two columns from the left) or σ_B (third column). The first column shows the σ_B data on the y-axis, while the last two show the w data.

and then dividing all shots in blocks with a fixed number of shots per block. However, the distributions of t and σ_B are not continuous (especially t , which is discretized), and it may be

2.3. PARAMETERS ANALYSIS

convenient to look for clustered data. The clustering approach can be implemented by the K-Means algorithm from the Scikit-Learn Python library, which lets us choose the number of clusters. The clustered data is shown in Fig. 2.3. The bubble parameters, averaged in each

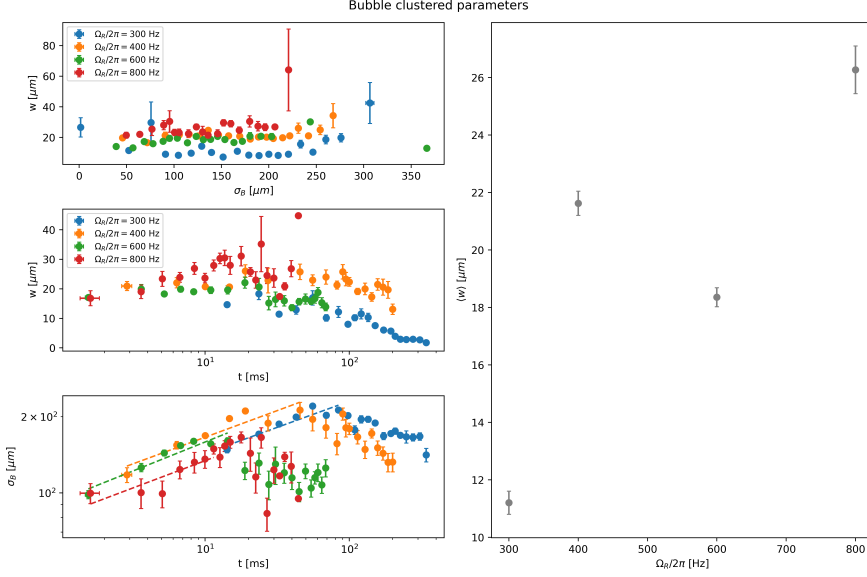


Figure 2.4: Bubble parameters distribution averaged on all shots of the same cluster. The left panel shows, from top to bottom, w vs σ_B , w vs t and σ_B vs t (the last one in log-log scale). In the last, a linear fit on the log-log increasing data is performed in order to estimate the rate of growth. The right panel presented the average tail width over all shots with the same coupling radiation Ω_R .

cluster and in relation one to another, are shown in Fig. 2.4, along with the average on all shots with the same radiation coupling. While the tail width looks constant when varying the bubble size, the bubble size is increasing with time at first, and then decreases. The initial behaviour corresponds to the power-law growth of σ_B in time of the type

$$\sigma_B(t) = At^B,$$

the final one is probability an artifact due to the low-density tails of the Thomas-Fermi distribution. Eventually, a linear fit is performed on the log-log data with the aim of finding the power-law coefficient B for each value of the radiation coupling, yielding

$$\begin{aligned} B_{300} &= 0.21 \pm 0.03, \\ B_{400} &= 0.21 \pm 0.04, \\ B_{600} &= 0.23 \pm 0.03, \\ B_{800} &= 0.22 \pm 0.06, \end{aligned}$$

all compatible among them, hence revealing that the bubble grows with the same profile at different values of Ω_R .

2.4 Spectral analysis

Since we are interested in the properties of the bubble throughout its evolution, periodic signals in the magnetization channel and their relation to the waiting time or the bubble size are important features to focus on. In order to study them, a spectral profile is much needed, from which one can extrapolate the main frequencies of the signals and, most importantly, the typical length scales of the system.

The tools used in the following analysis are the Fast Fourier Transform (FFT) and the auto-correlation function (ACF).

2.4.1 FFT and ACF definition

FFT We will first approach the problem of deriving such a profile by using the Fast Fourier Transform (FFT), an algorithm that implements the Discrete Fourier Transform (DFT) in an efficient manner.¹ Given the input as a sequence of N discrete values Z_0, \dots, Z_{N-1} sampled with spacing Δx , by definition the DFT is a series of N discrete values $\mathcal{F}_0, \dots, \mathcal{F}_{N-1}$ spaced by $\Delta k = 1/(N\Delta x)$ and convoluted with a complex phase such that

$$\mathcal{F}_k = \sum_{n=0}^{N-1} Z_n e^{-2\pi i \frac{k}{N} n}.$$

When the input Z_n is real-valued, the transform is too, and it is also symmetric between positive and negative frequencies. The physical world contains only positive frequencies, so we will neglect the negative part of the transform. This is achievable by using the Scipy function `rfft` instead of `fft`.

The result of the Fourier transform of a signal is the extraction of the main frequency components of the signal itself. In fact, as we know, the transform of a pure sinusoidal signal with frequency ω_0 results in a Dirac delta at $\omega = \omega_0$ (excluding the negative frequencies). In the general case of a signal made up of more frequency components and with noise, the peaks in the Fourier transform will correspond to the most relevant frequencies. Note that in our case the signal is in the space-domain, and by taking the inverse of the points in the frequency-domain, one can get information about the spatial periodicity of the system, hence the typical length scale.

ACF Another tool that can be used to study the periodic properties of a signal is the autocorrelation function (ACF). Similarly to the DFT, the ACF is also a particular type of convolution, where the signal is convoluted with itself. The caveat here is that since our signal is of finite length, the whole convolution would show boundary effects, as shown in Fig. 2.5. It is then worth limiting the signal in a central window of length $2W$ and computing the ACF on the windowed signal (Fig. 2.6). Taking as input the latter as Z_0, \dots, Z_{2W-1} , the output will be a series of values $\mathcal{A}_0, \dots, \mathcal{A}_W$ living in the space-domain² such that:

$$\mathcal{A}_k = \frac{1}{2} \left(\frac{\sum_n Z_n Z_{n+k}}{\sqrt{\sum_n Z_n^2 \sum_n Z_{n+k}^2}} + \frac{\sum_n Z_n Z_{n-k}}{\sqrt{\sum_n Z_n^2 \sum_n Z_{n-k}^2}} \right).$$

¹There are several efficient methods to compute the DFT. The most common implementation is the Cooley-Tukey algorithm, used in the Scipy Python library for FFT.

²While the FFT domain is made of frequencies, the ACF domain is instead made of lag values, corresponding to the spatial shifts of the signal.

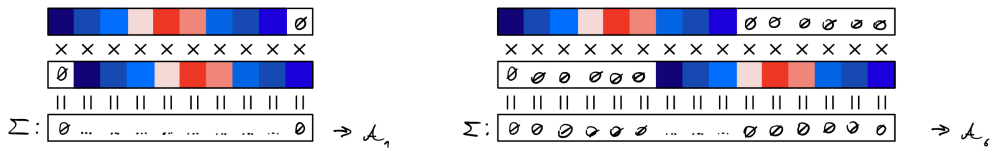


Figure 2.5: [TO IMPROVE] Schematic representation of boundary effects when computing the autocorrelation function on the whole signal. Since the signal is finite, the contributions on the borders are set to zero.

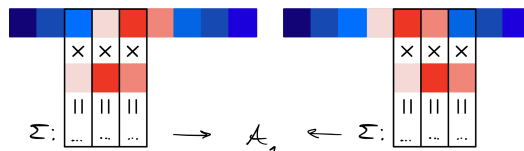


Figure 2.6: [TO IMPROVE] Schematic representation of windowed autocorrelation. In contrast to a full-width ACF, here no boundary effects arise.

This formula computes the windowed autocorrelation by shifting the signal both to the left and to the right and then taking the average. Both terms are normalized in order to get $A_0 = 1$. Note that the sums run from $n = 0$ to $n = W - 1$ and thus the length of the signal must be greater than $4W$: data that does not respect this condition will not be analyzed.

The computation of this function on some simple signals is shown in App. A. In contrast to the FFT, the ACF results, as mentioned before, live in the space-domain and give direct results on the length scales. A high ACF value at Δx_0 means that the signal is correlated with itself when shifted by Δx_0 . The periodicity of the signal is then related to the length Δx_0 .

2.4.2 FFT and ACF analysis on sequences

Now, what we shall do is computing the FFT and the ACF on the data, taking care of the fact that it is necessary to separate the inside region (the bubble) from the outside one. This is done by relying on the piecewise exponential fit results, namely the positions x_1 and x_2 from Eq. (2.4). An example of the inside region analysis for a selected pair of values Ω_R, δ (the same of Fig. 2.2) is presented in Fig. 2.7, where the data was first set to zero-mean and only the shots where $x_2 - x_1 > 4W$ are selected.

Let us briefly discuss the behaviours of the computed FFTs and ACFs, considering that it is similar for all sequences and the example presented is a good one (see Fig. 2.8, showing the profiles averaged over all sequences with the same Ω_R). The FFT shows a peak at a frequency in the order of $k_{\text{FFT}} \sim 0.01 \mu\text{m}^{-1}$ and of width in the order of $\Delta k_{\text{FFT}} \sim 0.1 \mu\text{m}^{-1}$. The ACF instead has a first peak at $\Delta x_{\text{ACF}} \sim 10 - 11 \mu\text{m}$. By comparing these results and relying on the FFT and ACF definitions, the relation should be $k \sim 1/\Delta x$. However, by taking the inverse of the ACF peak values, one gets $k_{\text{ACF}} \sim 0.1 \mu\text{m}^{-1}$, a frequency hidden in the FFT plot due to the broad peak. The reason for the peak broadness is probability the data noise, which is difficult to analyze properly. We will thus proceed by relying only on the ACF for the remaining analysis.

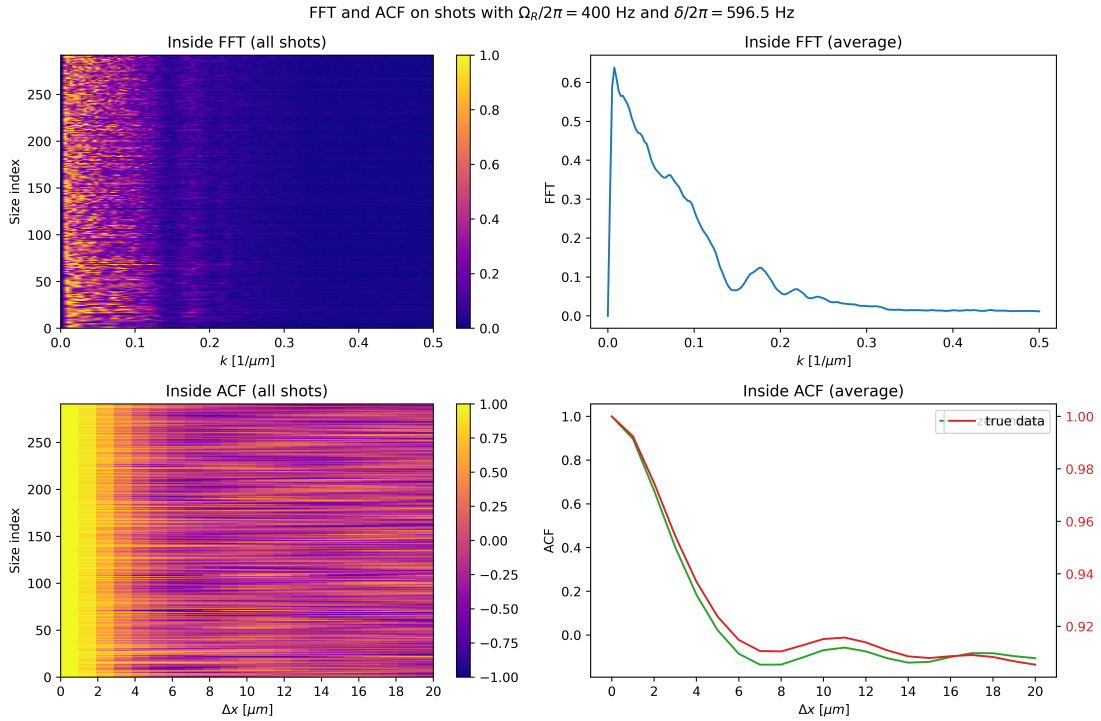


Figure 2.7: Example of FFT and ACF calculated on the inside region of shots with $\Omega_R/2\pi = 400$ Hz and $\delta/2\pi = 596.5$, after selecting the shots where $x_2 - x_1 > 4W = 80$. The values for each shot are shown in the left graphs with colormaps, while the averages on all shots are on the right. Note that before computing the transforms the data was set to zero-mean by subtracting its average. In the lower right graph, ACF computed on the true data (without the 0-mean) is shown for comparison to the other ACF profile.

2.4.3 ACF analysis on all shots

From now on, all shots will be considered, taking into account all Ω_R and δ values. What we shall proceed to do is studying the ACF parameters as functions of the bubble properties, such as the experimental waiting time and the bubble size, and of the experimental external parameters: the coupling Ω_R and the detuning δ . The routine is the following:

1. Gather all shots with the same Ω_R and save their bubble parameters;
2. Select only the shots where the inside or outside region is at least $4W$ pixels long;
3. Sort the shots based on the waiting time or the bubble size;
4. Cluster the shots based on the sorting parameter (as in Sec. 2.3);
5. Compute the ACF profile for each shot in a cluster and take the average;
6. Plot the ACF averages for each cluster and fit them;
7. Plot the fit results vs the time or size averages in each cluster.

The number of analyzed inside and outside shots is shown in Tab. 2.1.

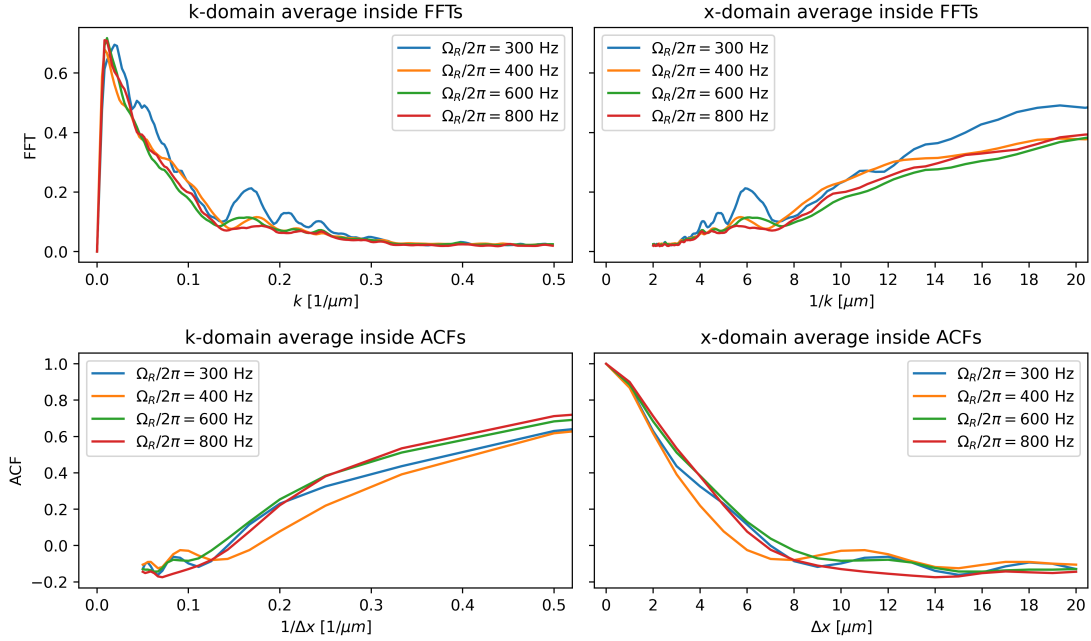


Figure 2.8: FFT and ACF profiles (computed with zero-mean data) averaged over all sequences with the same radiation coupling Ω_R . On the top, the FFTs are plotted both in the k -domain and x -domain. On the bottom, the ACFs are also plotted in the two domains to match the upper panel and confront the results. The FFTs are peaked at $k_{\text{FFT}} \sim 0.01 \mu\text{m}^{-1}$, while the first ACF peaks are at $\Delta x_{\text{ACF}} \sim 10 - 11 \mu\text{m}$.

$\Omega_R/2\pi$ [Hz]	# all shots	# inside shots	# outside shots
300	1491	1435	938
400	660	604	489
600	718	561	717
800	159	117	159

Table 2.1: Number of shots selected (where the inside or outside length is sufficient for the ACF computation). It is noticeable that the inside data for 300 Hz is way bigger than the rest.

Inside The ACF outside profiles can be fitted with a damped cosine of the form

$$\mathcal{A}_{\text{fit}}(x) = (1 - \Delta) \cos\left(\frac{x}{\ell_2}\right) \exp\left[-\left(\frac{x}{\ell_1}\right)^\alpha\right] + \Delta, \quad (2.5)$$

with $\alpha = 1.7$ fine-tuned in order to capture the profile in the best way possible.³ One could theoretically set α as a fit parameter, but this would result in a worse estimation of the length ℓ_1 , with the fit that adapts to the data by changing only α .

An example of fit on the inside shots is presented in Fig. 2.9, where the shots are grouped by time. The parameters retrieved from the fit are in Fig. 2.11 and 2.10. A global fit on all shots with the same radiation coupling is in Fig. 2.12. The size dependence seems to be the most

³Literature suggests to use $\alpha = 2$, a gaussian damping.

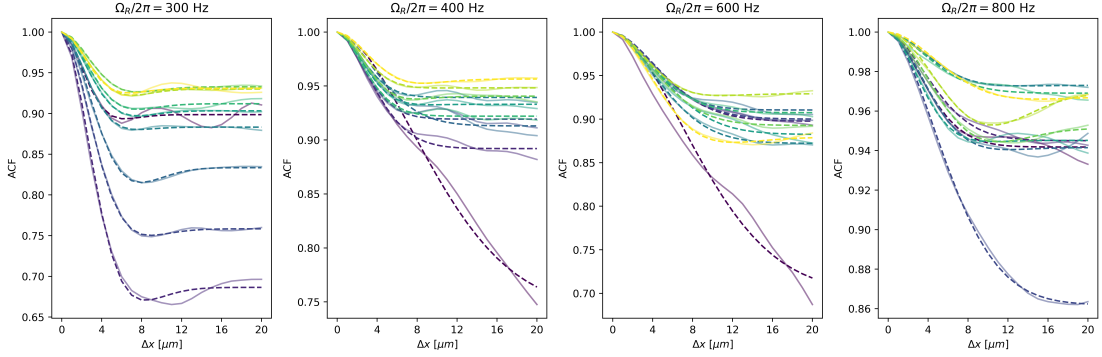


Figure 2.9: ACF average profiles of inside shots clustered by size in 10 blocks (solid lines) and fitted with the damped cosine of Eq. (2.5) (dotted lines) for each value of Ω_R . Size increases from darker to lighter colors.

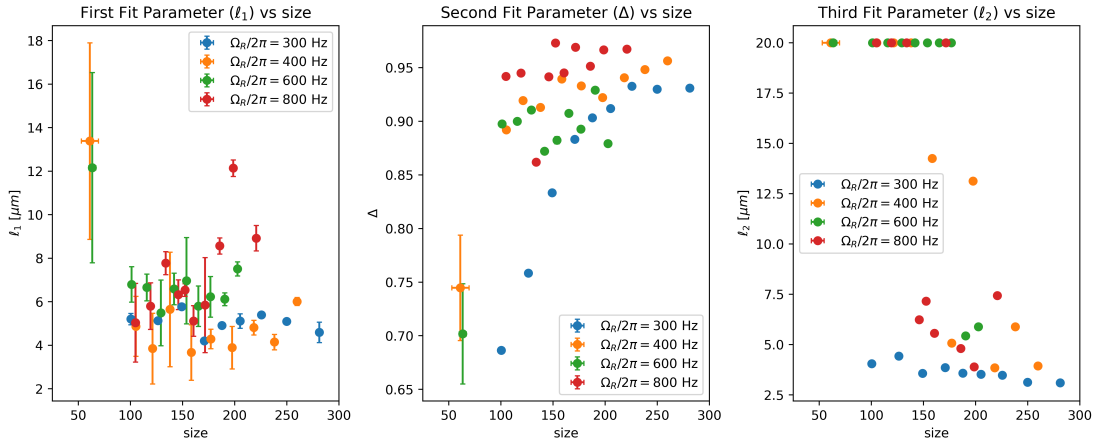


Figure 2.10: Fit parameters ℓ_1 , Δ and ℓ_2 of inside shots clustered by size (in log scale).

noticeable. From Fig. 2.10, the first parameter ℓ_1 is decreasing with size, while the second parameter Δ is increasing and approaching 1. This behaviour could mean that the magnetization inside the bubble loses (?) its spatial information with size.

Outside On the other hand, for the outside region ACF fit we use an exponential

$$\mathcal{A}_{\text{fit}}(x) = (1 - \Delta) \exp\left[-\frac{x}{\ell_1}\right] + \Delta. \quad (2.6)$$

An example of fit on the outside shots is presented in Fig. 2.13, where the shots are grouped by time. The parameters retrieved from the fit are in Fig. 2.15, 2.14. A global fit on all shots with the same radiation coupling is in Fig. 2.16. In contrast to the inside bubble region, what emerges outside the bubble is that the characteristic length of the autocorrelation ℓ_1 is increasing with size and the offset is decreasing (Fig. 2.15), which is the opposite behaviour.

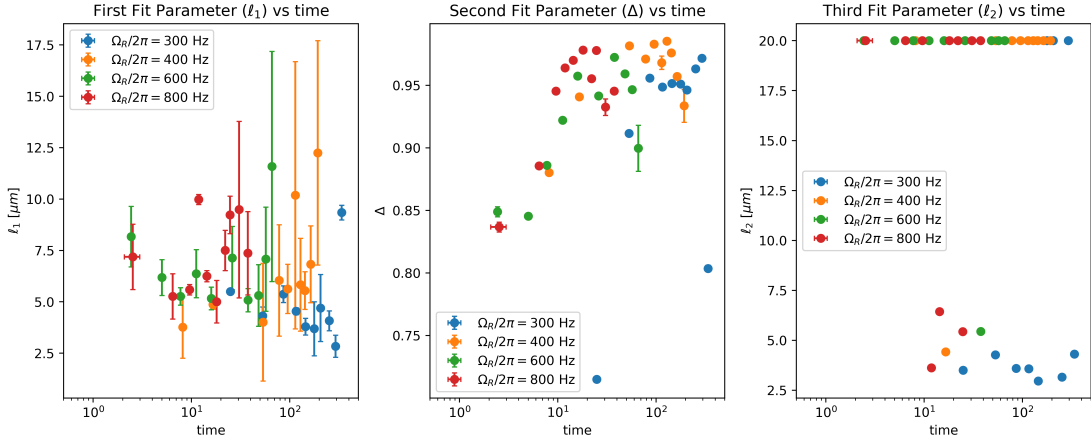


Figure 2.11: Fit parameters ℓ_1 , Δ and ℓ_2 of inside shots clustered by time (in log scale).

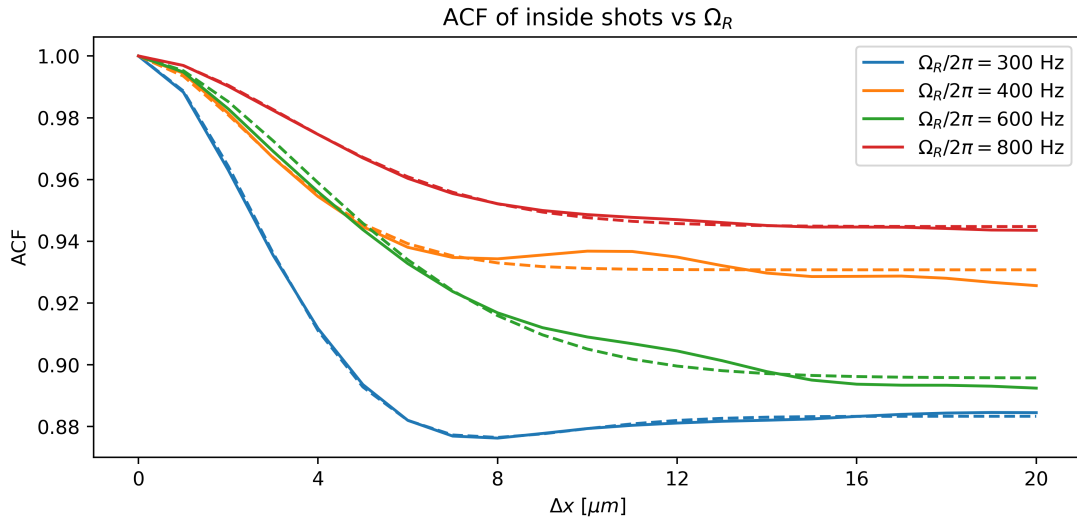


Figure 2.12: ACF average profiles of inside shots grouped by Ω_R (solid lines) and fitted with the damped cosine (dotted lines).

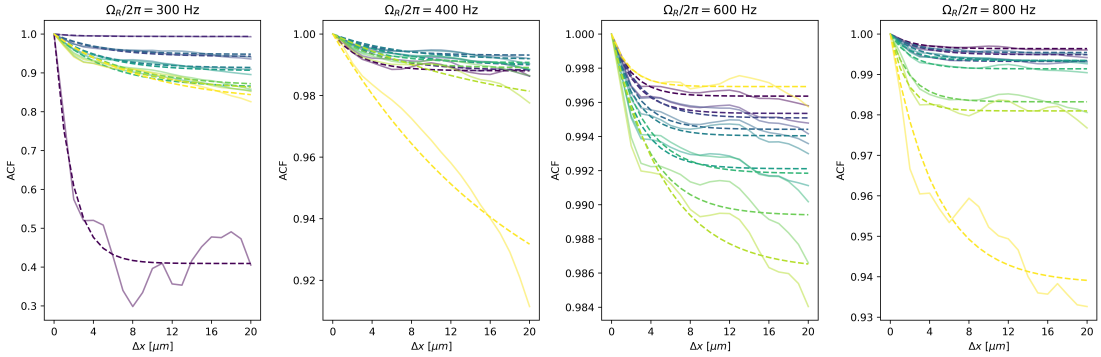


Figure 2.13: ACF average profiles of outside shots clustered by size in 10 blocks (solid lines) and fitted with the exponential of Eq. (2.6) (dotted lines) for each value of Ω_R . Size increases from darker to lighter colors.

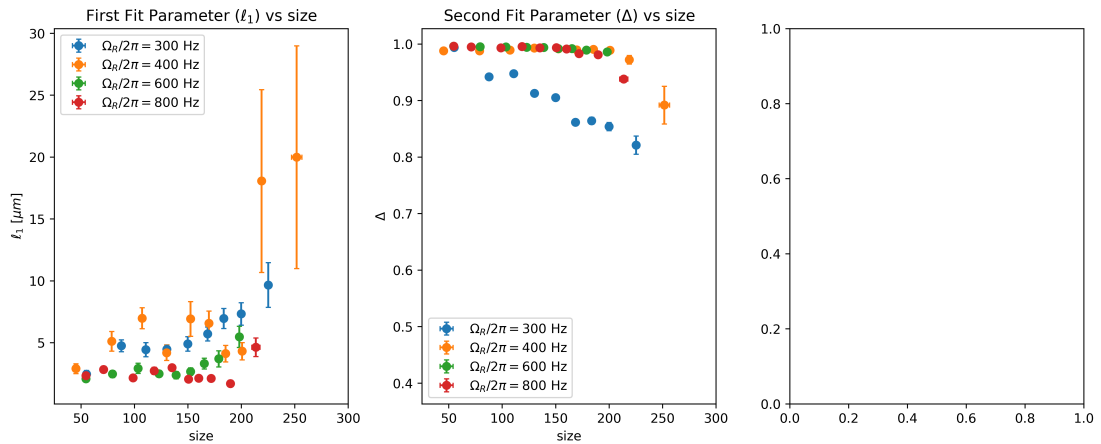


Figure 2.14: Fit parameters ℓ_1 and Δ of outside shots clustered by size.

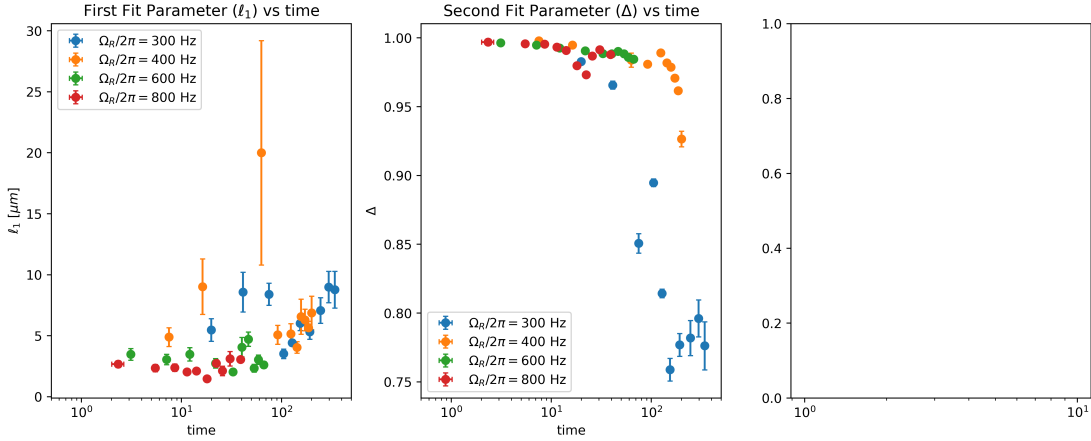


Figure 2.15: Fit parameters ℓ_1 and Δ and of outside shots clustered by time (in log scale).

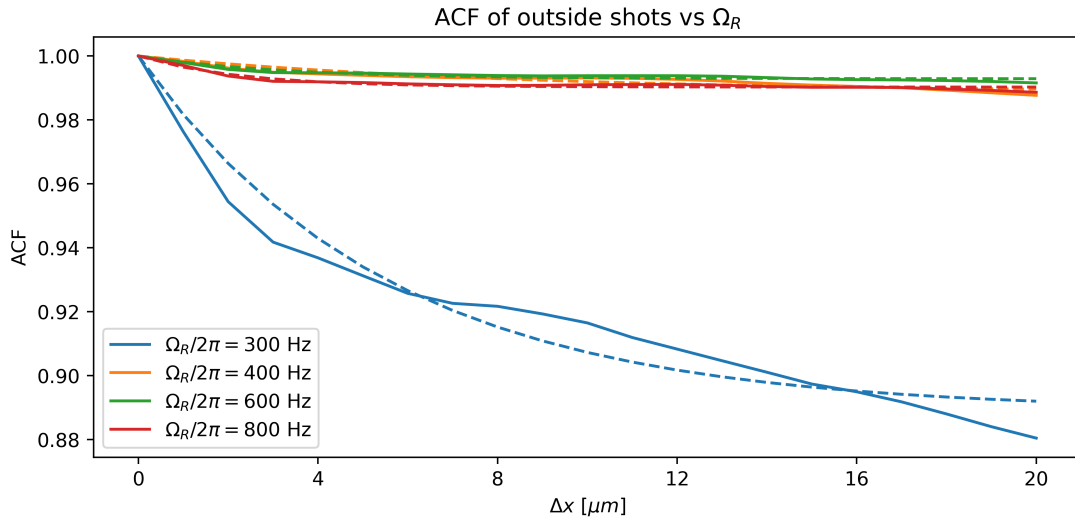


Figure 2.16: ACF average profiles of outside shots grouped by Ω_R (solid lines) and fitted with the exponential (dotted lines).

CHAPTER 2. DATA ANALYSIS

Conclusions

CONCLUSIONS

Appendix A

ACF models

The autocorrelation function is a powerful tool for a spectral analysis of the data, since it can extract the main frequency of the signal. Let us compute the expected model for the ACF in some example cases, using the function

$$\mathcal{A}(m) = \frac{1}{2} \left(\frac{\sum_n f_n f_{n+m}}{\sqrt{\sum_n f_n^2 \sum_n f_{n+m}^2}} + \frac{\sum_n f_n f_{n-m}}{\sqrt{\sum_n f_n^2 \sum_n f_{n-m}^2}} \right) \quad (\text{A.1})$$

and supposing to run the sums over N values covering many periods of the signal $f(x)$.

A.1 Pure sinusoid

First, let us take a pure sinusoidal signal

$$f(x) = A \cos(k_0 x + \phi),$$

where x can be discretized with $x = x_0 + n\Delta x$, yielding

$$f_n = A \cos[k_0(x_0 + n\Delta x) + \phi].$$

When considering Eq. (A.1), the left and right contributions shall be treated separately (the calculation is eventually the same). We then proceed with the calculation of $S(m) = \sum_n f_n f_{n+m}$:

$$S(m) = \sum_n A^2 \cos[k_0(x_0 + n\Delta x) + \phi] \cos[k_0(x_0 + (n+m)\Delta x) + \phi],$$

where we can use the trigonometric identity

$$\cos(\alpha) \cos(\beta) = \frac{1}{2} [\cos(\alpha - \beta) + \cos(\alpha + \beta)]$$

getting

$$S(m) = \frac{A^2}{2} \sum_n [\cos(k_0 m \Delta x) + \cos(k_0 (2x_0 + (2n+m)\Delta x) + 2\phi)].$$

The second term in the sum averages to zero, but the first one survives and does not depend on n , hence

$$S(m) = \frac{A^2}{2} N \cos(k_0 m \Delta x).$$

APPENDIX A. ACF MODELS

What is left to compute are the normalization sums $\sum_n f_n^2$ and $\sum_n f_{n+m}^2$. But since the cosine squared averages to $\frac{1}{2}$ over one period, the result is straight-forward and both sums are equal to $\frac{A^2}{2}N$. Eventually, the ACF right term reads

$$\mathcal{A}(m) = \frac{\frac{A^2}{2}N \cos(k_0 m \Delta x)}{\sqrt{\frac{A^2}{2}N \frac{A^2}{2}N}} = \cos(k_0 m \Delta x),$$

and since Δx is fixed, the ACF lets us extrapolate the signal frequency k_0 .

Bibliography

- [1] Giacomo Lamporesi. "Two-component spin mixtures". In: *arXiv preprint arXiv:2304.03711* (2023).
- [2] Lev Pitaevskii and Sandro Stringari. *Bose-Einstein condensation and superfluidity*. Vol. 164. Oxford University Press, 2016.
- [3] Alessandro Zenesini et al. "False vacuum decay via bubble formation in ferromagnetic superfluids". In: *Nature Physics* (2024), pp. 1–6.

BIBLIOGRAPHY

List of Figures

1.1	GPE simulation of a two-component balanced mixture in a harmonic potential. The shaded purple region shows the density distribution of population a and the yellow one the population b . Here, a small magnetic field is used to break the left-right symmetry. The total density profile is drawn in black.	6
1.2	Mean field energy and bubble formation.	7
2.1	Example of fit results performed on a shot. First, the data is fitted with the double-arctangent function of Eq. (2.2), then each shoulder is fitted with a single-arctangent, namely the one of Eq. (2.3). This ensures a better estimation of the shoulder centers and thus of the bubble width. Eventually, a last fit is done with the piecewise function of Eq. (2.4), in order to capture the inside/outside discontinuity and the exponential tails.	11
2.2	Example of initial shot sorting based on experimental waiting time (on the left) and final sorting based on bubble width σ_B (on the right) for all shots with $\Omega_R/2\pi = 400$ Hz and $\delta/2\pi = 596.5$ Hz. The σ_B parameter is estimated from the previous fitting procedure, and the no-bubble shots ($\sigma_B = 0$) are removed from the right plot. The data is colored by mapping positive magnetization to blue and negative magnetization to red.	11
2.3	Data clustering with the K-Means algorithm and $n_{\text{clusters}} = 20$ based only on t (first two columns from the left) or σ_B (third column). The first column shows the σ_B data on the y-axis, while the last two show the w data.	12
2.4	Bubble parameters distribution averaged on all shots of the same cluster. The left panel shows, from top to bottom, w vs σ_B , w vs t and σ_B vs t (the last one in log-log scale). In the last, a linear fit on the log-log increasing data is performed in order to estimate the rate of growth. The right panel presented the average tail width over all shots with the same coupling radiation Ω_R	13
2.5	[TO IMPROVE] Schematic representation of boundary effects when computing the autocorrelation function on the whole signal. Since the signal is finite, the contributions on the borders are set to zero.	15
2.6	[TO IMPROVE] Schematic representation of windowed autocorrelation. In contrast to a full-width ACF, here no boundary effects arise.	15

LIST OF FIGURES

2.7	Example of FFT and ACF calculated on the inside region of shots with $\Omega_R / 2\pi = 400$ Hz and $\delta / 2\pi = 596.5$, after selecting the shots where $x_2 - x_1 > 4W = 80$. The values for each shot are shown in the left graphs with colormaps, while the averages on all shots are on the right. Note that before computing the transforms the data was set to zero-mean by subtracting its average. In the lower right graph, ACF computed on the true data (without the 0-mean) is shown for comparison to the other ACF profile.	16
2.8	FFT and ACF profiles (computed with zero-mean data) averaged over all sequences with the same radiation coupling Ω_R . On the top, the FFTs are plotted both in the k -domain and x -domain. On the bottom, the ACFs are also plotted in the two domains to match the upper panel and confront the results. The FFTs are peaked at $k_{\text{FFT}} \sim 0.01 \mu\text{m}^{-1}$, while the first ACF peaks are at $\Delta x_{\text{ACF}} \sim 10 - 11 \mu\text{m}$	17
2.9	ACF average profiles of inside shots clustered by size in 10 blocks (solid lines) and fitted with the damped cosine of Eq. (2.5) (dotted lines) for each value of Ω_R . Size increases from darker to lighter colors.	18
2.10	Fit parameters ℓ_1 , Δ and ℓ_2 of inside shots clustered by size (in log scale).	18
2.11	Fit parameters ℓ_1 , Δ and ℓ_2 of inside shots clustered by time (in log scale).	19
2.12	ACF average profiles of inside shots grouped by Ω_R (solid lines) and fitted with the damped cosine (dotted lines).	19
2.13	ACF average profiles of outside shots clustered by size in 10 blocks (solid lines) and fitted with the exponential of Eq. (2.6) (dotted lines) for each value of Ω_R . Size increases from darker to lighter colors.	20
2.14	Fit parameters ℓ_1 and Δ of outside shots clustered by size.	20
2.15	Fit parameters ℓ_1 and Δ and of outside shots clustered by time (in log scale).	21
2.16	ACF average profiles of outside shots grouped by Ω_R (solid lines) and fitted with the exponential (dotted lines).	21